J. Eur. Opt. Society-Rapid Publ. 2026, **22**, 1

https://doi.org/10.1051/jeos/2025050
Available online at: https://jeos.edpsciences.org

Journal of the European Optical Society-Rapid Publications

RESEARCH ARTICLE OPEN ACCESS

Experimental demonstration of optical energy transfer between the 0th and −1st orders diffracted by an all-dielectric resonant waveguide grating

Rosa Olloghe Mandoukou[1], Maxime Royon[1,*], Arnaud Meyer[1], Maxime Darnon[1], Irvin Girault[1], Damien Jamon[1], William Ravisy[2], Gerges El Haber[2], Laurent Dubost[2], Samuel R. De Cotret[3], Oleh Fesiienko[3], Isabelle Verrier[1], and Yves Jourlin[1]

[1] Laboratoire Hubert Curien, UMR 5516, UJM, CNRS, IOGS, 18 rue du Professeur Benoit Lauras, 42000 Saint-Etienne, France
[2] HEF IREIS, ZI Sud – Avenue Benoit Fourneyron, 42160 Andrézieux-Bouthéon, France
[3] Institut Interdisciplinaire d'Innovation Technologique (3IT), Parc Innovation (P2-3000) 3000, Boulevard de l'Université, Sherbrooke, Canada

Received 4 November 2025 / Accepted 26 November 2025

Abstract. The energy transfer between the reflected 0th and −1st orders diffracted by a grating in the vicinity of the Littrow angle is experimentally demonstrated for the first time with an all-dielectric resonant waveguide grating under TE polarization. This effect has already been described in a theoretical approach but never proved by measurements. Contrary to classical configuration, the dielectric resonant diffractive structure is probed here from the grating backside to avoid signal disturbance. A transparent layer of very high refractive index (hydrogenated amorphous silicon: a-Si:H) is structured by e-beam lithography and plasma etching to create a resonant grating waveguide on a BK7 substrate. Agreement between modeling and experimental characterizations validates the energy transfer effect, opening the way to all-dielectric sensing devices.

Keywords: Resonant waveguide grating, Energy transfer, Hydrogenated amorphous silicon.

1 Introduction

In the past years, a large number of optical sensors based on plasmonic devices were described in the literature and have taken an important place for environmental or biological applications [1–3]. One means to couple light to plasmon waves and to achieve surface plasmon resonance is the use of metallic diffraction gratings under TM polarization [3, 4]. Generally, only the 0th reflected order is exploited to detect a change in the dielectric medium by the determination of the minimum in the angular or spectral signal [5]. However, to improve the device sensitivity, we previously demonstrated that the −1st reflected order diffracted by the grating can be useful when measured simultaneously with the 0th reflected order [6, 7]. The energy transfer between these two orders when tuning the wavelength or the incident angle, based on a lossless coupling of surface plasmonic modes, can be exploited as a highly sensitive sensor [8, 9]. Differential measurement of these two orders reduces the common mode noise and therefore improves sensitivity of the sensors based on this effect. Nevertheless, the device can only be probed from the grating top, meaning that the incident light and the reflected orders are perturbed by the medium to be tested, mainly when one considers liquid environment. To avoid this limitation, we propose here an all-dielectric structure that allows probing from the backside (substrate). The aim of this study is to demonstrate that, like for plasmonic sensors, it is possible to simultaneously use the 0th and −1st diffraction orders and that their energy transfer is possibly exploitable for a sensing system. To the best of our knowledge, this configuration represents the first realization of such an approach, opening new possibilities for advanced biosensor design.

In Section 2, the energy transfer is described briefly for the backside probing case and an explanation of the whole dielectric structure behavior is conducted. Section 3 is dedicated to the materials and methods to optimize the grating design and to fabricate the samples. Finally, Section 4 presents and discusses experimental results and is followed by a conclusion.

2 Optical energy transfer between the 0th and −1st grating orders

A diffraction grating is used in the present work to obtain, through an-all dielectric configuration, an optical energy

* Corresponding author: maxime.royon@univ-st-etienne.fr

transfer between the 0th and −1st orders when scanning the incidence angle. The structure, as it is well-known in resonant waveguide grating (RWG) will then support guided modes and will exploit waveguide resonance in high refractive index dielectric [10] with the aim to use this device as sensor. The main difference with other works [11–13] is that the incident light, studied in TE polarization, is coming from the backside of the grating (from the substrate) in order to avoid disturbance effects from the external medium to be probed (Fig. 1). In this case, resonant reflected orders will be also retrieved from the same side (substrate) than the incident beam one.

As mentioned in [14] in a theoretical point of view, the waveguide and the grating must be in a high refractive index material for the energy transfer to occur between the two reflected −1st and 0th orders only, when scanning the incident angle in the vicinity of the Littrow angle (θ_L, angle for which the reflected −1st order is superposed to the incident light). This condition is essential to avoid any transmitted order from having a propagating character in the external medium and to couple the evanescent diffracted orders to the guided modes. Several other parameters are conditioning the optical energy transfer existence, in particular the grating geometry. The following subsections aim to describe how the guided modes could propagate in the resonant structure and how they can be excited by the grating to obtain optical energy transfer between the two reflected orders.

2.1 Mode's propagation in the waveguide

The resonant grating is partially etched in a high refractive index medium layer n_{wg} deposited on the substrate of refractive index n_s, as represented in Figure 2. The grating shows here a square profile with a depth d, a period Λ and a duty cycle $(1-f)$. The underneath layer (buffer layer), as part of the waveguide, has a thickness W_g. The superstrate refractive index is n_{super} (Fig. 2a) and corresponds to the refractive index of the medium to be probed (liquid or air).

To understand how the resonant structure behaves, an equivalent structure is considered in Figure 2b. It is composed of only one high refractive index plane layer, sandwiched between the substrate and superstrate. Its total thickness is noted $w_{\text{eqTOTAL}} = W_g + d_{\text{eq}}$ where d_{eq} is the equivalent thickness corresponding to the top grating and which can be written as:

$$d_{\text{eq}} \cdot n_{\text{wg}} = d \cdot n_{\text{eq}}, \tag{1}$$

where n_{eq} is the equivalent refractive index of the plane layer that is substituted for the grating. n_{eq} is dependent of the incident wave polarization (TE or TM) according to Rytov's formulas [15]. In the case of air as superstrate ($n_{\text{super}} = n_{\text{air}} = 1$) and with $f = 0.5$, it follows for TE polarization:

$$w_{\text{eqTOTAL,TE}} = w_g + d_{\text{eq,TE}} = w_g + d/n_{wg}\sqrt{\frac{\left(n_{wg}^2+1\right)}{2}}. \tag{2}$$

To create a guided mode in the waveguide equivalent structure of refractive index n_{wg}, the plane wave propagating in

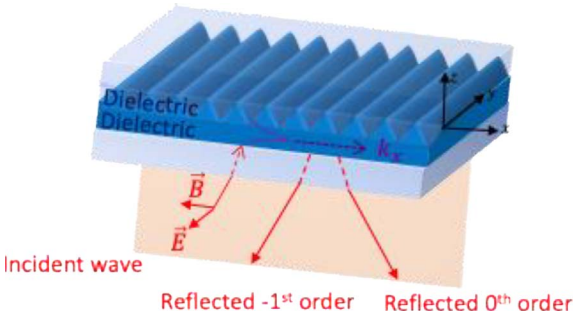

Figure 1. Excitation of the guided mode by the dielectric diffraction grating.

the direction of the wave vector $\vec{k_{wg}}$ ($||\vec{k_{wg}}|| = \frac{2\pi}{\lambda} n_{wg}$) under α angle should interfere constructively with itself (Fig. 2c). This condition leads to the dispersion equation of the lth guided TE mode when introducing the mode effective refractive index $n_e = n_{wg}cos\alpha$:

$$l\pi = \frac{1}{2}\left(\varphi_{\frac{wg}{s}} + \varphi_{\frac{wg}{\text{super}}}\right) + \frac{2\pi}{\lambda} w_{\text{eqTOTAL}}\sqrt{{n_{wg}}^2 - n_e^2}, \tag{3}$$

where $\varphi_{\frac{wg}{s}}$ and $\varphi_{\frac{wg}{\text{super}}}$ are the phases due to the total reflection at the substrate and superstrate boundaries, expressed for TE polarization by:

$$\begin{cases} \varphi_{\frac{wg}{s}} = -2\text{atan}\left(\sqrt{\dfrac{n_e^2 - n_s^2}{n_{wg}^2 - n_e^2}}\right), \\ \varphi_{\frac{wg}{\text{super}}} = -2\text{atan}\left(\sqrt{\dfrac{n_e^2 - n_{\text{super}}^2}{n_{wg}^2 - n_e^2}}\right). \end{cases}$$

The number of modes supported by the equivalent structure can be determined versus waveguide thickness w_{eqTOTAL} and wavelength λ from the dispersion equation (3). For TE polarization, the l-mode cut-off happens when $n_e = n_s$ ($n_s > n_{\text{super}}$) below which value the mode could not propagate anymore:

$$\left(\frac{w_{\text{eqTOTAL}}}{\lambda}\right)_{\text{TE}_{\text{cut-off}}} = \frac{l\pi + \text{atan}\left(\sqrt{\frac{n_s^2 - n_{\text{super}}^2}{n_{wg}^2 - n_s^2}}\right)}{2\pi\sqrt{n_{wg}^2 - n_s^2}}. \tag{4}$$

Under an appropriate incident angle, the TE_0 mode could be excited in the resonant structure for $l = 0$ if the waveguide equivalent thickness is above its corresponding cut-off. For different incident angles, other modes ($l > 0$) can be guided if increasing the waveguide equivalent width. It can lead to optical energy transfer between the 0th and −1st orders if the grating geometry is adapted to excite the mode. The grating coupling to the guided modes is described in the following paragraph.

2.2 Guided modes excitation by the grating diffraction orders

The TE modes will propagate in the waveguide at a speed associated to their effective indices $n_e = n_{wg}\cos\alpha$ and will be

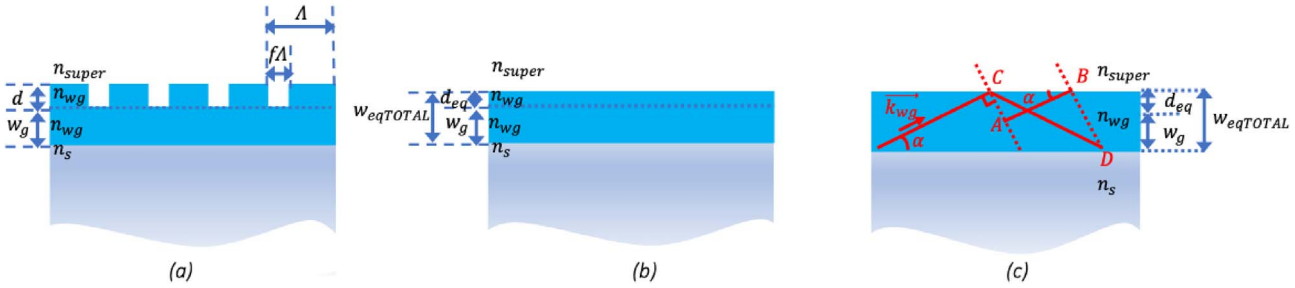

Figure 2. (a) Studied resonant structure, (b) Equivalent plane structure, (c) Mode propagation in the equivalent structure.

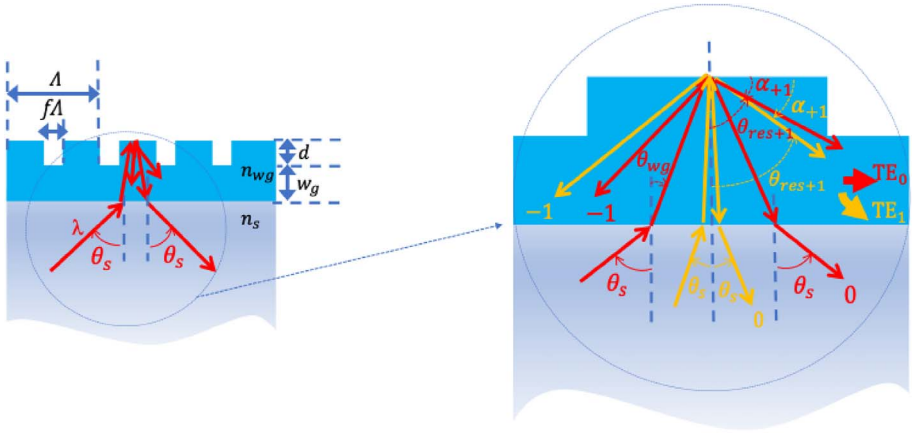

Figure 3. Excitation of the guided modes by the grating in the dielectric structure.

excited by the reflected waves diffracted by the grating at the angles $\theta_{\text{res}} = \pi/2 - \alpha$, leading to resonance effects. Using the grating equation, the resonant angles θ_{res} and the corresponding effective refractive indices n_e are defined for each diffracted order m by equation (5):

$$n_e = \sin(\theta_{\text{res}})\, n_{wg} = \sin(\theta_{wg})\, n_{wg} + m\frac{\lambda}{\Lambda} = \sin(\theta_s)\, n_s + m\frac{\lambda}{\Lambda}. \quad (5)$$

θ_{wg} is the incident angle on the grating in the waveguide and θ_s is the incident angle coming from the substrate for the resonance (Fig. 3).

Under appropriate grating geometry, at a small incident angle (yellow), the $l = 1$ propagating mode (TE$_1$) can be excited in the waveguide by the $m = +1$ diffracted order and at a higher incident angle (red), the $l = 0$ propagating fundamental mode (TE$_0$) can also be excited by the same order $m = +1$. The $m = -2$ evanescent order could also excite the $l = 0$ counter-propagating mode (TE$_0$) at a higher angle. The energy transfer arises in between these two last angles.

To summarize, the energy transfer in all-dielectric resonant structure will appear under several conditions linked to the opto-geometrical parameters of the resonant structure: the wavelength, the polarization, the waveguide width, the depth, period and duty cycle of the grating and finally the refractive indices of the materials constituting the resonant structure. The choice of these parameters is discussed in the following section to design a full dielectric optical energy transfer device.

3 Material and methods

3.1 a-Si:H deposition and characterization

To fulfill the required condition of no transmitted orders for the energy transfer, a high refractive index material (>3) is necessary. Additionally, to achieve the best performance and to obtain high resonances efficiencies, the material should exhibit a high transparency at the operating wavelength due to the specific interrogation of the developed sensor (from the substrate to the resonant grating). With a dielectric constant above 3 and an extinction coefficient below 0.01 in IR wavelength range, hydrogenated amorphous silicon (a-Si:H) meets this criterium. The characterization of a-Si and a-Si:H was largely investigated in the literature [16–20]. This particular material is largely used in the solar cell technology and many techniques can be used to deposit a-Si:H layers (plasma spray, reactive chemical vapor deposition, sputtering,...) [21]. The passivation of defects, responsible for optical losses in the visible and IR domain, by forming Si-H bonds, enables a high transparency. For instance, a-Si:H layers with refractive index

as high as 3.44 can be obtained in the IR range while the material is transparent (absorption coefficient $k = 0$) [17]. These optical constants can be tuned by controlling the amorphous degree of Si and the concentration of Hydrogen [18]. Therefore, a-Si:H was chosen as the material that constitutes the resonant structure. The fabrication and the characterization of the layer are described in the following sections.

3.1.1 a-Si:H deposition

The deposition of hydrogenated amorphous silicon (a-Si:H) films is performed using magnetron sputtering in an industrial-scale TSD-550 machine from HEF Durferrit. The chamber is equipped with a magnetron sputtering cathode of Si (99.99%) operated in pulsed direct current (pDC) mode in the tens of kilohertz range, with argon and hydrogen gas lines respectively for sputtering gas and hydrogenation of the material. The H_2/Ar gas ratio was fixed to 0.9 and the pDC power to 1 kW. The substrates were placed on a barrel-type substrate holder with a diameter of 550 mm and were heated at 573°K before and during deposition.

3.1.2 Ellipsometric measurements

Figure 4 shows the dispersion function of an a-Si:H layer on a BK7 substrate determined by spectroscopic ellipsometry. The refractive index values (blue curve) are around $n_{wg} = 3.5$ and the absorption coefficient values (green curve) below 0.0038 above 800 nm wavelength, meaning that a-Si:H layer is almost transparent above 800 nm with high enough refractive index. Considering that the response of silicon-based photodetectors is maximum between 800 nm and 1 µm and that compact laser diodes emitting at 980 nm are available, the operating wavelength of the device is set to 980 nm. At $\lambda = 980$ nm, the refractive index and the absorption coefficient values are $n_{wg} = 3.562$ and $k_{wg} = 0.0036$, respectively. The layer's thickness deduced from the ellipsometric measurements is equal to 336.65 ± 0.03 nm. These parameters are of great importance for prediction of the optical angular response to determine the best grating geometry leading to the optimized energy transfer as explained in Section 3.2.

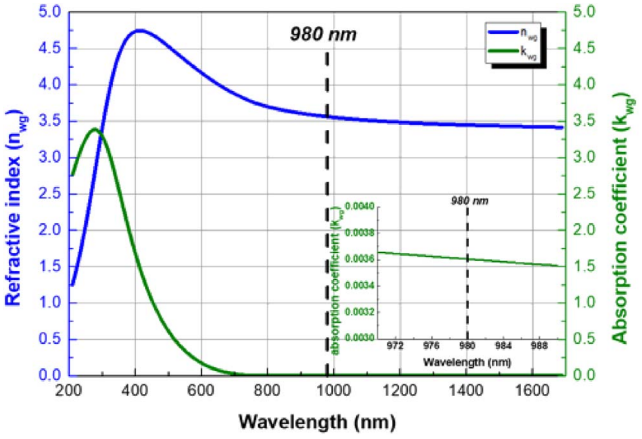

Figure 4. Ellipsometric measurements resulting from the hydrogenated amorphous silicon deposition (a-Si:H). The blue curve represents the refractive index and the green line the absorption depending on wavelength. At the operating wavelength $\lambda = 980$ nm, the refractive index is $n_{wg} = 3.562$ and the absorption coefficient $k_{wg} = 0.0036$.

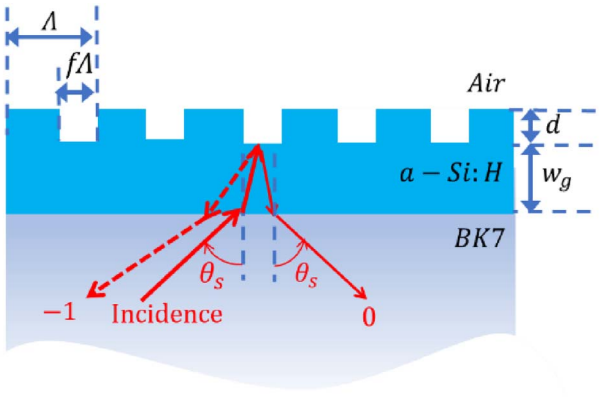

Figure 5. Structure used to model the interaction of a TE-polarized light beam emitting at 980 nm wavelength with a BK7 substrate above which a thin layer of a-Si:H is deposited and grooved.

3.2 Grating design

3.2.1 Resonant structure scheme: fixed parameters

Once the refractive index, the thickness of the a-Si:H layer and the operating wavelength are fixed, we used the "MC Grating" software [22] based on the Rigorous Coupled Wave Analysis (RCWA) method to design the optimized structure, comprising the grating and the under layer, and to calculate its optical response.

Figure 5 shows the binary grating design with the structure parameters used for the simulation. The TE-polarized light at wavelength 980 nm is incident from the substrate before impinging into the a-Si:H. As recommended for probing from back-side (substrate), the transmission medium index (air, $n_{\text{super}} = 1$) is lower than those of the incident medium corresponding here to the substrate (BK7, $n_s = 1.508$) and the a-Si:H waveguide refractive index ($n_{wg} = 3.562$) is larger than the one of the substrate.

The period and the duty cycle are fixed to $\Lambda = 390$ nm and $f = 0.5$, respectively. For this period, the Littrow angle $\theta_L = \text{asin}(\lambda/((2\ n_s\Lambda))) = 56.44°$ is above the critical angle $\theta_c = \text{asin}(n_{\text{super}}/n_s) = 42°$, which cancels the 0th transmitted order.

3.2.2 Parameters to optimize

Thicknesses Wg and d must be determined considering that the total thickness of a-Si:H layer ($d + Wg = 337$ nm) is imposed by the layer deposition requirements (see §.3.1). The 0th and −1st orders efficiencies versus these two parameters are mapped in Figure 6 at the Littrow angle ($\theta_s = \theta_L = 56.44°$ in the BK7 substrate). The 0th and −1st orders efficiencies show minima (Fig. 6a) and maxima

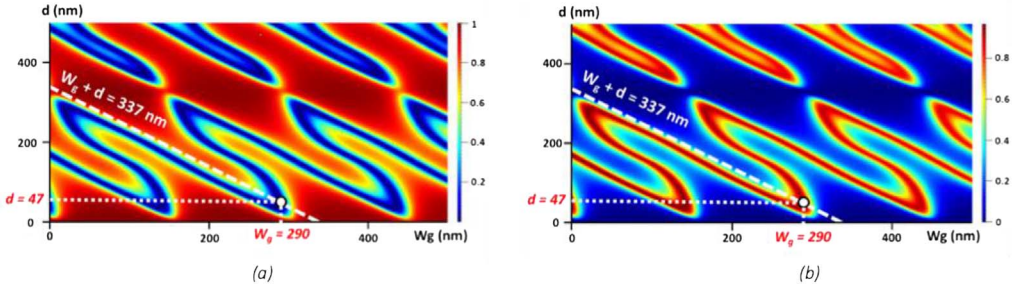

Figure 6. 2D maps efficiencies as a function of the grating depth d and waveguide thickness Wg for $\theta_L = 56.44°$: (a) 0th order, (b) −1st order.

(Fig. 6b), respectively, for given couples values (Wg, d), which indicates a maximum energy transfer between the two orders. The white line in Figures 6a and 6b corresponds to the total thickness $d + Wg = 337$ nm and its intersection with minimum for the 0th order and maximum for the −1st order provides the optimal couple values $d = 47$ nm, $Wg = 290$ nm (white point) for the energy transfer.

3.2.3 Angular response of the optimized structure

Using the optimized structure with a TE-polarized light excitation at wavelength 980 nm, on an angular range between $0° < \theta_s < 90°$ into the BK7 substrate and between $0° < \theta_{wg} < 25°$ into the a-Si:H layer, the diffraction efficiencies are plotted in the Figure 7 where both orders 0 and −1 are represented in black and red line, respectively. Points of interest are also represented, especially the resonances at positions A and B corresponding to 5.2° and 33.4° angles. Then, the efficiency curves intersect each other at C and E corresponding to 44.1° and 76.2° angles, which are relevant for further sensing measurements. Position D corresponds to the Littrow's angle $\theta_L = 56.44°$. Above 44° (position C), the energy transfer between the 0th and −1st orders is obtained and at the Littrow angle specifically, their respective efficiencies reach 0 (minimum for the 0th order) and 0.9 (maximum for the −1st order).

Knowing the optimal values allowing a good energy transfer between the 0th and −1st orders, the grating fabrication process can now be carried out as described in the next section.

3.3. Gratings fabrication

After deposition of a-Si:H on the BK7 substrate, the gratings are formed by a combination of e-beam lithography and plasma etching, performed at 3IT.Nano facilities, Sherbrooke, QC, Canada.

3.3.1 E-beam

A layer of 150 nm-thick positive electroresist (Zep520A) is spun onto the sample, followed by a thin metallic layer evaporated on the resist to evacuate charges and to adjust focus during exposure. The patterns are exposed using an EBPG e-beam lithography tool from Raith operating at 100 kV. The design corresponds to a 10 × 10 mm^2 grating

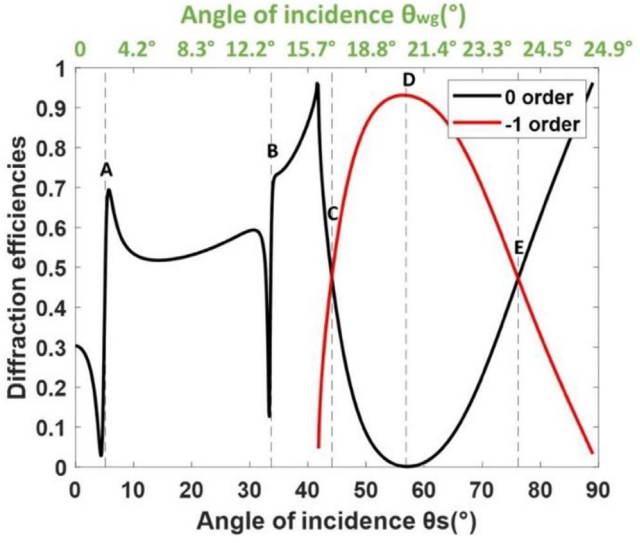

Figure 7. Computed efficiencies in TE-polarization of the −1st (red curve) and the 0th (black curve) orders versus incident angle for a square grating of 390 nm period, 0.5 duty cycle, 47 nm depth and 290 nm waveguide thickness: θ_s angular position into the BK7 substrate (black axis values) and θ_{wg} into the a-Si:H layer (green axis values) with characteristic angles at A, B, C, D and E.

with a period of 390 nm and a line width of 195 nm (see Sect. 3.2). Writing fields of 100 × 100 µm^2 were used to reduce stitching effects and ensure smoothness along the grating's direction. After exposure, the metallic layer is removed by an acidic bath that does not affect the resist. Development is performed in ZED-N50 solution at 4 °C and dried with a nitrogen jet.

3.3.2 Plasma etching

Following electron-beam lithography, the resulting patterns are transferred into the amorphous silicon (a-Si:H) layer via plasma etching using a $CF_4/H_2/He$ gas mixture in an Advanced Oxide Etcher (AOE) system from SPTS. The etching duration is determined empirically through iterative trials to achieve the targeted etch depth of approximately 47 nm. Subsequently, residual photoresist is

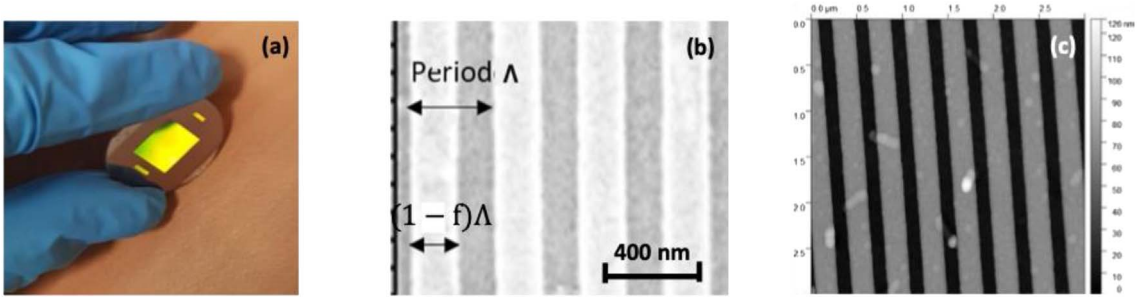

Figure 8. (a) Photograph of the grating etched with e-beam with (b) SEM surface characterization (c) AFM image.

removed by O_2 plasma treatment performed within the same etching tool. Finally, the sample undergoes ultrasonic cleaning in isopropyl alcohol for 10 min, followed by thorough rinsing with deionized water and drying with a nitrogen jet.

3.3.3 Characterization of manufactured samples

After etching, morphological characterizations by AFM and SEM are carried out to precisely determine the grating geometry (Fig. 8). These measurements reveal an average period of $\Lambda = 390$ nm, a depth $d = 69$ nm ($Wg = 268$ nm) and a duty cycle $(1-f) = 0.57$, values which slightly differ from the optimized parameters found previously ($\Lambda = 390$ nm, $d = 47$ nm, $Wg = 290$ nm, $1-f = 0.5$). Despite this discrepancy attributed to the fabrication deviations, the following section will present how the structure behaves for energy transfer between the −1st and 0th orders with the real geometry of the manufactured grating.

4 Results and discussion

4.1 Simulated optical response of the fabricated structure

The actual grating dimensions have been input in the modeling software to verify that the optical energy transfer is still obtained between the two orders above the incident angle $\theta_s > 40°$ in the BK7 layer. Figure 9 shows that even though the amplitudes efficiencies difference of the 0th and the −1st orders is smaller than those of the optimized structure for the Littrow angle, the actual structure still provides an optical energy transfer between angles 40° and 90°. Despite the difference between the optimized and the real structure, the energy transfer can still theoretically be exploited, as demonstrated in the experimental part below.

For each relevant incident angles, A, B, C and E, Figure 10 illustrates the incident and the reflected beams propagation in the direct space as well as in the reciprocal space (Ewald's sphere) and the electrical field distribution in the resonant structure to identify respective guided modes. To do this, an angle conversion from the substrate to the a-Si:H layer is necessary. Figures 10a and 10b show three reflected diffracted orders (0, −1 and +1) inside the

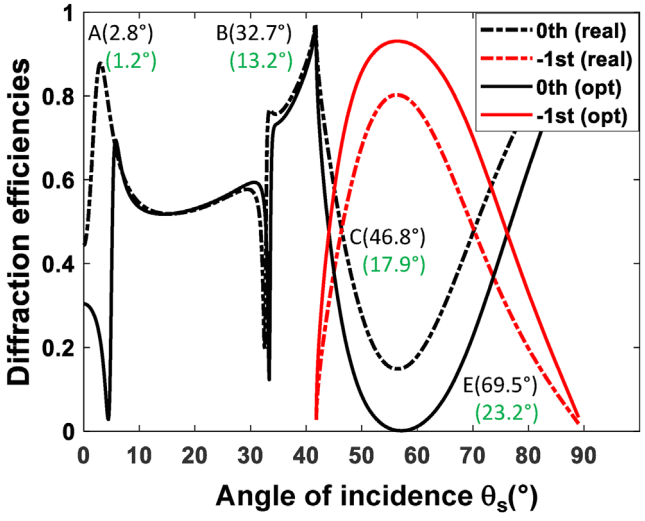

Figure 9. Comparison between the computed −1st (red curves) and the 0th (black curves) orders efficiencies in TE-polarization versus incident angle θ_s into the BK7 substrate for a square grating of 390 nm period. Full line: depth $d = 47$ nm, waveguide thickness $Wg = 290$ nm and duty cycle $f = 0.5$; dotted line: $d = 69$ nm, $Wg = 268$ nm, $f = 0.57$. For A, B, C and E, θ_s (θ_{wg} into the a-Si:H layer) are mentioned in black (green).

a-Si:H layer. For point A ($\theta_s = 2.8°$), the 0th order is transmitted in the superstrate (air) and the +1st order excites the TE_1 mode that propagates in the guide with an effective index $n_e = 2.59$ as seen in the Ewald sphere in the Figure 10a and visible on the electric field E_y amplitude map. The reflected −1st order cannot escape from the a-Si:H layer and is not transmitted back into the substrate. For point B ($\theta_s = 32.7°$), the 0th order is partially reflected into the a-Si:H layer and transmitted in the substrate (BK7) and the +1st order excites the TE_0 mode that propagates in the guide with an effective index $n_e = 3.33$ (Fig. 10b). The reflected −1st order can still not come out of the a-Si:H layer and is not transmitted into the substrate. For the first and the second crossing points C ($\theta_s = 46.8°$, Fig. 10c) and E ($\theta_s = 69.5°$, Fig. 10d), there is no phase matching between the diffracted evanescent orders and the propagating modes in the waveguide but the electric field is partially present in the superstrate above

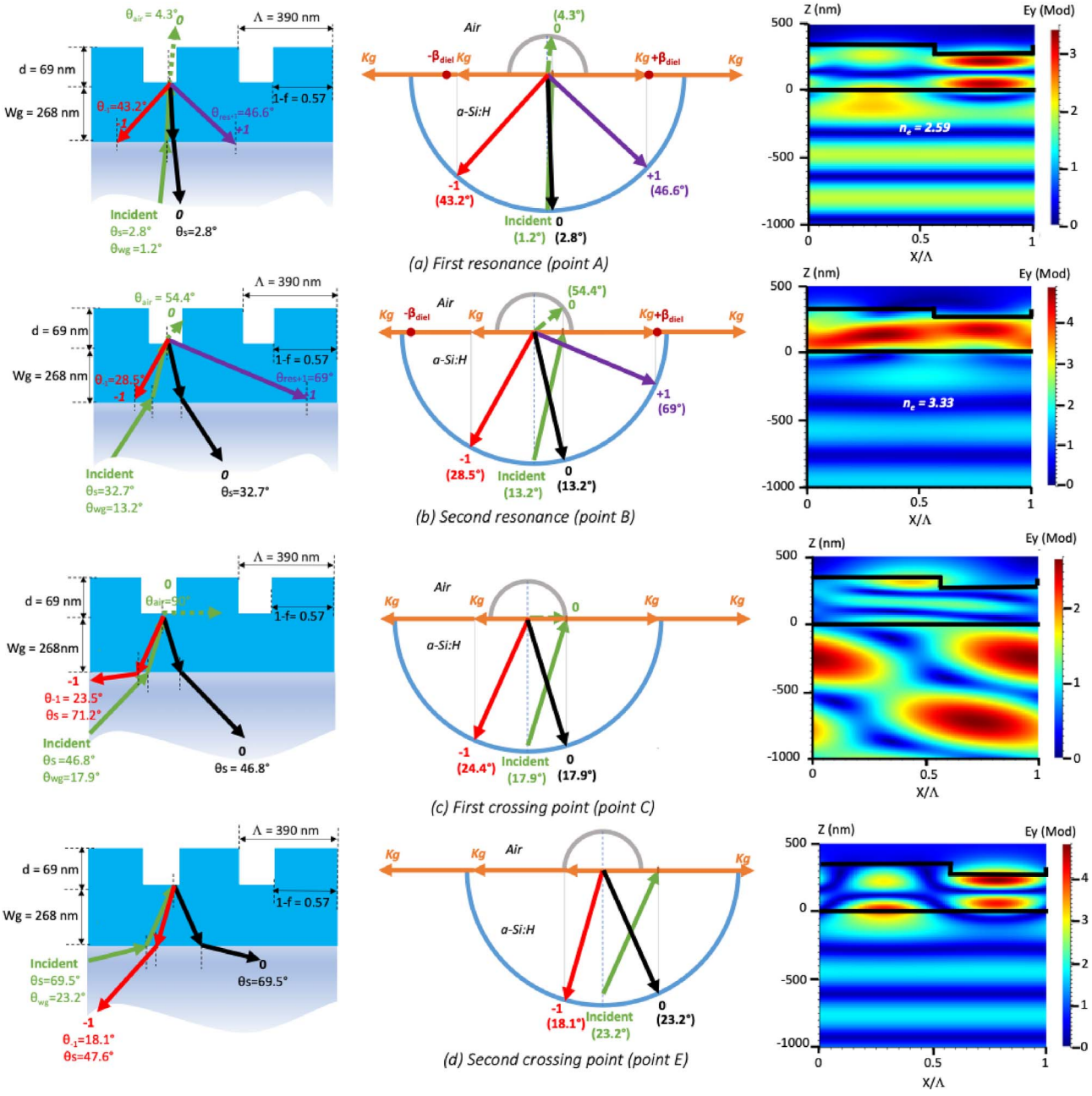

Figure 10. Schemes in direct and reciprocal (Ewald sphere's representation) spaces associated to angular positions of the Figure 3 and electric field E_y amplitude: (a) First resonance at $\theta_s = 2.8°$ (point A), (b) Second resonance at $\theta_s = 32.7°$ (point B), (c) First crossing point $\theta_s = 46.8°$ (point C) and (d) Second crossing point $\theta_s = 69.5°$ (point E).

the grating for an eventual probing of the surrounding medium refractive index change.

4.2 Angular measurements

4.2.1 Optical setup

The angular response corresponding to the measurement of the propagative reflected orders intensities (0th and −1st), looking like an eye shape in the Littrow angle vicinity and called "switch eye", is measured by an optical bench schematized in Figure 11a. The collimated beam emitted at wavelength 980 nm is provided by a laser diode and passes through a diaphragm for spatial filtering and through a polarizer to ensure TE-polarization according to the grating incidence plane. The laser diode, diaphragm and polarizer are set on a same rotative support and the photodiode is mounted on another motorized rotation stage. According to the incident angle on the grating, both 0th and −1st orders are diffracted and their efficiencies are measured sequentially by the photodiode, converting intensity into a current that is sent to the analog input of

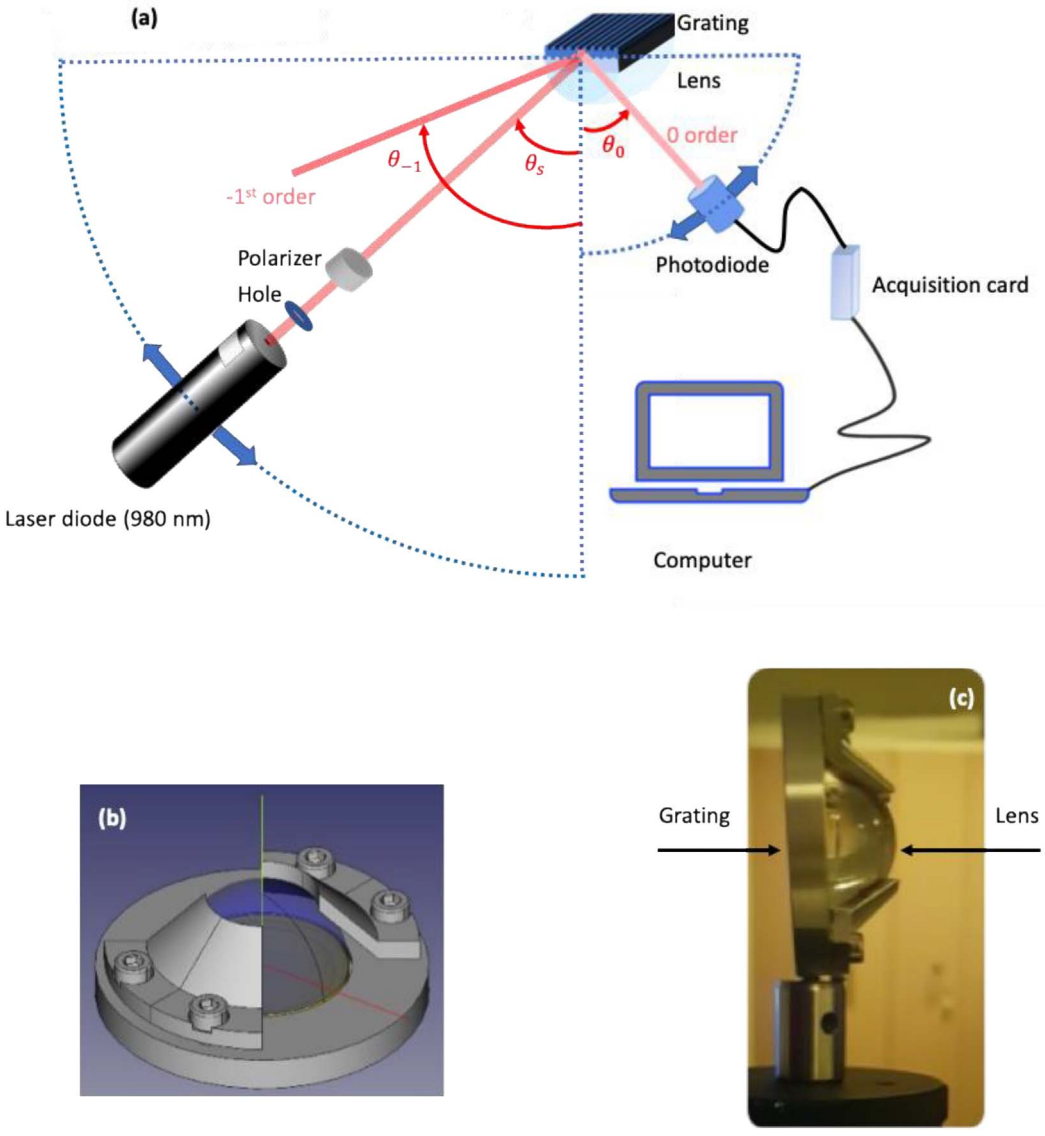

Figure 11. (a) Angular characterization bench, (b) Side view of the sample and half sphere holder, (c) Photograph of the holder designed to maintain the half sphere and the sample.

an acquisition card connected to a computer, which stores the intensities for each incident angle. The grating is probed by the laser diode from the back side as shown in Figure 1.

Direct measurement of the angular response on the whole range of 0°–90° is impossible due to the high refractive index of the resonant waveguide layer that leads to total internal reflection at BK7 substrate and a-Si:H interface.

To ensure the angular scanning by the incident beam within the resonant structure, a half sphere with the same refractive index as the substrate is added with an index-matching fluid on the back side of the substrate to couple the light from the air to the a-Si:H grating with a grazing angle between 40° and 80°. To support the grating and the half sphere, a holder was specially designed as shown in Figures 11b and 11c. The sphere must be properly positioned on the characterization bench so that the incident beam is centered with no tilt in normal incidence. The grating is also rotated in its support to have the diffracted orders in the horizontal plane.

4.2.2 Experimental results

After optical alignments, measurements were carried out to verify the ability of the sample to exhibit an energy transfer between the 0th and −1st diffracted orders. For each incident angle θ_s from 0° to 70° with a step of 1°, controlled by the laser diode rotation stage, the 0th order and the −1st order diffraction intensities are measured by the photodiode. Experimental values (points in black and in red for the 0th and −1st orders respectively) are plotted in Figure 12 and superimposed to the theoretical curves (thin lines) simulated with the actual grating parameters values.

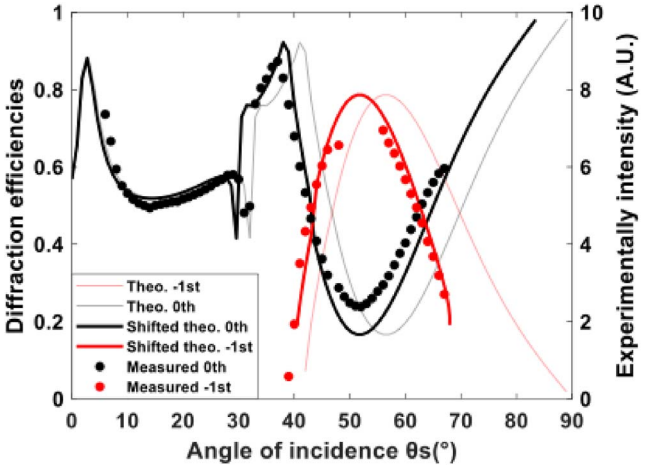

Figure 12. 0th (black) and −1st (red) orders diffraction efficiencies measurements (points) and theoretical curves (lines), the grating period is 390 nm, the depth 69 nm, the duty cycle 0.57 and the waveguide thickness 268 nm.

The simulated and experimental curves are quite similar for low incidence angles ($\theta_s < 38°$); resonances appear at the same angles for the 0th reflected order ($\theta_s = 2.8°$ for point A and $\theta_s = 33°$ for point B), but for $\theta_s > 38°$, an increased shift of the experimental values is observed towards smaller incident angles. The first intersecting point (C) and the second (E) appear experimentally at $\theta_s = 44°$ and $\theta_s = 61°$ instead of 46.8° and 69.5° theoretically. The angle corresponding to the 0th and −1st orders extrema efficiencies is also experimentally smaller than the theoretical Littrow angle ($\theta_s = 51°$ instead of 56°). The greater is the incident angle, the angular shift increases. This shift is explained by the opto-geometrical configuration of the experimental set-up since the reflected 0th and −1st orders are not centered on the half sphere center. As shown in Figure 13, the output angles θ_e and θ_{e-1} of the reflected 0th and −1st orders are determined by the substrate refractive index $n_s = 1.5$ and its thickness $t = 1$ mm (BK7) and to the BK7 half sphere radius $R = 12.7$ mm by the equation (6) obtained by geometric optics calculations:

$$\begin{cases} \theta_e - \theta_s = \theta_1 - \theta_2 = \Delta_0 \\ \theta_{-1d} - \theta_s = \Delta_{-1} \end{cases} \quad (6)$$

with $n_s \sin\theta_1 = \sin\theta_2$, $R\sin\theta_1 = 2t\sin\theta_s$, $R\sin\theta_{-1d} = t\cos\theta_s(\tan\theta_{ds} - \tan\theta_s)$ and $\left(\sin\theta_{ds} = \sin\theta_s - \frac{\lambda}{\Lambda n_s}\right)$. This leads to an angular shift for the first and second crossing points of $\Delta_0 = \Delta_{-1} = 3°$ and $\Delta_0 = \Delta_{-1} = 4°$ respectively. Similarly, the Littrow angle is calculated to be shifted by $\Delta_0 = \Delta_{-1} = 4°$ from its actual value. Experimentally, the angular shifts at these different points are in close agreement with the calculated ones. The shifted theoretical curves are plotted in thick lines (black and red for the 0th and −1st orders) in Figure 12 and correspond to the experimental data although the half sphere and the index-matching fluid introduce aberrations that become more significant as the incidence angle increases.

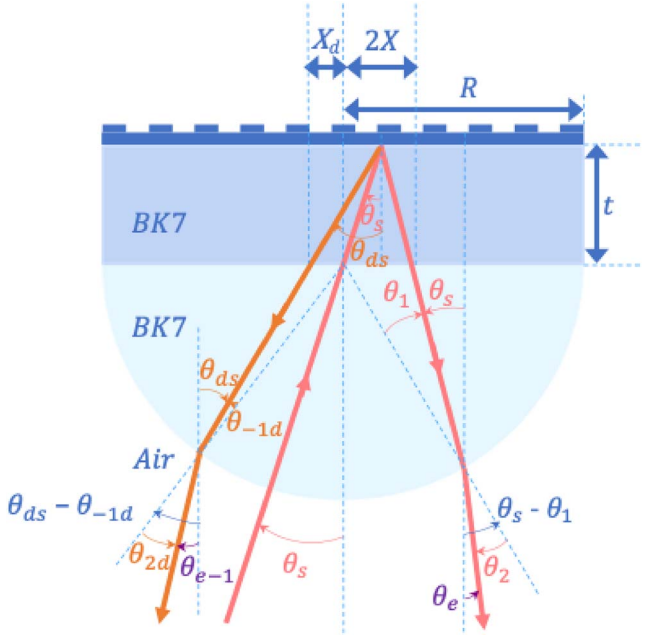

Figure 13. 0th and −1st reflected orders paths when taking into account the substrate thickness t and the half-sphere.

In addition, compared to the theoretical curve, the relative amplitudes of both orders are experimentally lower than the prediction; in other words, the efficiencies are less important than expected. Furthermore, the grating profile may not be perfectly square and its roughness was not considered in the simulation, which may lead also to reduce diffracted orders efficiencies due to optical losses. Nevertheless, the experimental proof of the energy transfer is clearly demonstrated, showing the two expected intersection angles at C and E positions between 0th and −1st reflected orders efficiencies and energy transfer in between them. These two particular angles could then be used for optical sensing in future applications. Since their corresponding efficiencies can be unbalance due to a change in the medium to be probed, its refractive index variation can be measured at these two angles. This configuration and implementation will be exploited in further developments as a highly sensitive refractometry-based sensor.

5 Conclusion

A comprehensive study has demonstrated the feasibility of optical energy transfer between the 0th and −1st orders diffracted by a grating in all-dielectric resonant structure. Using optimized a-Si:H layers, which combine a high refractive index with low infrared absorption, the structure was fabricated via e-beam lithography and plasma etching, and its angular diffraction behavior was experimentally characterized. For the first time, such a structure was shown to allow energy transfer between the 0th and −1st diffraction orders, while conventional high-index materials (e.g., TiO_2, HfO_2, Si_3N_4) do not allow this effect because higher-order diffracted modes arise within the guiding layer

in the transmitted medium. These results confirm both theoretically and experimentally the potential of this approach where the grating is probed through the substrate bottom. Further development will aim to leverage this optical energy transfer at the two crossing angles for sensing application such as detection of gaseous species. This topic will be addressed in a forthcoming article where its performances will be evaluated (sensitivity, optical losses...). Another point to consider is the possibility of avoiding the use of the half sphere to couple light in the resonant structure, in order to reduce aberrations and to propose a compact and miniaturized optical sensor.

Acknowledgments

The authors thank Professor Olivier Parriaux for the fruitful discussions about the switch effect, Frédéric Arnould for mechanical part of the experimental bench and Laboratoire Nanotechnologies Nanosystèmes (LN2) for supporting the fabrication costs.

Funding

This work was supported by the LABEX MANUTECH-SISE (ANR-10-LABX-0075) of Université de Lyon, within the Plan France 2030 operated by the French National Research Agency (ANR).

This work has been funded by a public grant from the French National Research Agency (ANR) under the "France 2030" investment plan, which has the reference EUR MANUTECH SLEIGHT -ANR-17-EURE-0026.

This work has been partially funded by Laboratoire Nanotechnologies Nanosystèmes (LN2).

Conflicts of interest

The authors have nothing to disclose.

Data availability statement

Data associated with this article are available from the corresponding author upon reasonable request.

Author contribution statement

Conceptualization, Y.J., I.V, R.O.M, L.D, and M.R.; Methodology, Y.J., I.V, R.O.M, M.D., and M.R.; Software, I.G., M.R., I. V., A.M., and R.O.M.; Validation, R.O.M., M.R., A.M., M.D, D.J., W.R., G.E.H., I.V., and Y.J.; Formal Analysis, R.O.M., M. R., A.M., M.D., D.J., W.R., G.E.L., L.D., I.V., S.D.C., O.F., and Y.J.; Resources, R.O.M, M.R., A.M., M.D., W.R., G.E.H., L.D., S.D.C., O.F., I.V., and Y.J.; Data Curation, R.O.M, M.R., A.M., M.D., D.J., I.V., and Y.J.; Writing – Original Draft Preparation, R.O.M, M.R., M.D., I.V., and Y.J.; Writing – Review & Editing, R.O.M, M.R., A.M., M.D., G.E.H, S.D.C, O.F., I.V., and Y.J.; Visualization, R.O.M., M.R., M.D., I.V., and Y.J.; Supervision, I.V., M.R., L.D., and Y.J.; Project Administration, I.V., M.R., and Y.J.; Funding Acquisition, M.R.

References

1 Maier SA, Plasmonic : Fundamentals and Applications, edited by Springer US (Springer, US, 2007). https://doi.org/10.1007/0-387-37825-1.
2 Homola J, Surface plasmon resonance sensors for detection of chemical and biological species, Chem. Rev. 108, 462 (2008). https://doi.org/10.1021/cr068107d.
3 Dostálek D, Homola J, Miler M, Rich information format surface plasmon resonance biosensor based on array of diffraction gratings, Sens. Actuators, B Chem. 107, 154 (2005). https://doi.org/10.1016/j.snb.2004.08.033.
4 Cao J et al., The sensitivity of grating-based SPR sensors with wavelength interrogation, Sensors. 19, 405 (2019). https://doi.org/10.3390/s19020405.
5 Cai H et al., Theoretical and experimental study of a highly sensitive SPR biosensor based on Au grating and Au film coupling structure, Opt. Express. 30, 26136 (2022). https://doi.org/10.1364/OE.461768.
6 Bruhier H et al., Theoretical investigation of refractive index detection limit in the surface plasmon resonance-triggered switch effect, IEEE Sens. J. 24, 40659 (2024). https://doi.org/10.1109/JSEN.2024.3485245.
7 Laffont E et al., Development of a new plasmonic transducer for the detection of biological species, in Proceedings of the SPIE Photonics Europe conference, Proc. SPIE 12139, Optical Sensing and Detection VII, 121390 B (2022). https://doi.org/10.1117/12.2619331.
8 Giraud P, et al., Ppb detection level's hydrogen sensor using a SPR grating in the triggered switching configuration, Opt. Express. 33, 29648 (2025). https://doi.org/10.1364/OE.561549.
9 Bruhier H et al., Common-mode plasmon sensing scheme as a high-sensitivity compact SPR sensor, Opt. Lett. 48, 3733 (2023). https://doi.org/10.1364/OL.483692.
10 Quaranta G et al., Recent advances in resonant waveguide gratings, Laser Photonics Rev. 12, 1800017 (2018). https://doi.org/10.1002/lpor.201800017.
11 Wang SS, Magnusson R, Theory and applications of guided-mode resonance filters, Appl. Opt. 32, 2606 (1993). https://doi.org/10.1364/AO.32.002606.
12 Wang SS et. al., Guided-mode resonances in planar dielectric layer diffraction gratings, J. Opt. Soc. A. 7, 1470 (1990). https://doi.org/10.1364/JOSAA.7.001470.
13 Vermeulen N et al., Low-loss wavelength tuning of a mid-infrared Cr2+:ZnSe laser using a Littrow mounted resonant diffraction grating, Laser Phys. Lett. 8, 606 (2011). https://10.1002/lapl.201110044.
14 Parriaux O, Jourlin Y, Lossless 0th and −1st order switching by dual-excitation of grating waveguide mode, J. Opt. 21, 075603 (2019). https://doi.org/10.1088/2040-8986/ab252a.
15 Rytov SM, Electromagnetic properties of a finely stratified medium, Sov. Phys. JETP. 2, 466 (1956).
16 Volodin VA, Koshelev DI, Quantitative analysis of hydrogen in amorphous silicon using Raman scattering spectroscopy, J. Raman Spectrosc. 44, 1760 (2013). https://doi.org/10.1002/jrs.4408.
17 Huang Y et al., UV-Raman scattering of thin film Si with ultrathin silicon oxide tunnel contact for high efficiency crystal silicon solar cells, Sol. Energy Mater. Sol. Cells. 192, 154 (2019). https://doi.org/10.1016/j.solmat.2018.12.025.
18 Pierce DT, Spicer WE, Electronic structure of amorphous Si from photoemission and optical studies, Phys. Rev. B. 5, 3017 (1972). https://doi.org/10.1103/PhysRevB.5.3017.
19 Yang Y et al., Revealing structural disorder in hydrogenated amorphous silicon for a low-loss photonic platform at visible frequencies, Adv. Mater. 33, 2005893 (2021). https://doi.org/10.1002/adma.202005893.

20 Swanepoel R, Determination of the thickness and optical constants of amorphous silicon, J. Phys. E. 16, 1214 (1983). https://doi.org/10.1088/0022-3735/16/12/023.
21 Stuckelberger et al., Review: Progress in solar cells from hydrogenated amorphous silicon, Renew. Sustain. Energy Rev. 76, 1497(2017). https://doi.org/10.1016/j.rser.2016.11.190.
22 Lyndin N, Usievich B, MC Grating. (2013). https://mcgrating.com/.